TPAC V1 Paper

J. A. Ballin*, J. P. Crooks†, P. D. Dauncey*, A.-M. Magnan*, Y. Mikami‡, O. D. Miller‡, M. Noy*, V. Rajovic‡, M. M. Stanitzki†, K. D. Stefanov†, R. Turchetta†, M. Tyndel†, E. G. Villani†, N. Watson‡, J. A. Wilson‡

July 28, 2008

Abstract

ECAL, CMOS blah.

*Department of Physics, Blackett Laboratory, Imperial College London, London.
†STFC, Rutherford Appleton Laboratory, Chilton, Didcot.
‡School of Physics and Astronomy, University of Birmingham, Birmingham.

Contents

1 Introduction - ~ 2 pages

In this paper, we present results from a test sensor which was designed to investigate a novel approach to electromagnetic calorimeters (ECAL). In this, the readout of the ECAL is binary, meaning that each channel returns a yes/no result with no further amplitude information.

The sensor is based on a $0.18\,\mu$m CMOS process, which was modified to include a "deep p-well" implant. This modified process is called INMAPS and is described elsewhere [**?**]. This protects signal charge from absorption by the circuit electronics and so allows a significant amount of signal processing and data handling in the pixels.

Although the potential applications for a binary ECAL are wide, the sensor discussed in this paper was designed for a specific application, namely the International Linear Collider (ILC) [**?**]. This is widely assumed to be the next worldwide particle physics frontier accelerator. It has a wide and rich physics programme [**?**].

Many of the measurements require reconstruction of heavy decaying particles into hadrons. To identify the decaying particles through the invariant mass of the hadronic jets requires excellent hadronic jet energy resolution. The main technique which should give this resolution are Particle Flow Algorithms (PFA) [**?**] which require very high granularity calorimetry to allow the separation of the showers from the individual particles in the jet. For the ECALs, it is widely accepted that a sampling calorimeter will provide the best PFA performance, due to both transverse and longitudinal granularity. The current state-of-the-art has silicon sensors as the detecting layers and tungsten as the converter.

In this paper, the rest of this section expands on the requirements for the ILC application. The test sensor is described in Sec 3. ETC.

2 Requirements - ~ 5 pages

2.1 Electromagnetic shower properties

An electron, positron or photon interacting in material produces an electromagnetic (EM) shower containing a large number of electrons, positrons and photons. A sampling EM calorimeter (ECAL) measures the charged particle component of the shower at various positions in shower depth by having sensitive layers interspersed with the dense material which efficiently produces the shower. The sensitive layers operate by measuring the ionisation created by the charged particles in these layers and normally the shower energy is estimated by measuring the energy deposited through the ionisation.

In this paper, we present a new technique for a sampling ECAL, in which an estimate of the number of particles in the shower is used as the measure of the shower energy, rather than the energy deposited. Clearly, these quantities are strong correlated, as each charged particle in the shower will deposit energy in the sensitive layer. However, the energy deposited depends on the speed and angle of the charge particle and also has fluctuations around the average deposit, as described by the Landau function. Hence, it would be expected that the energy deposited would have a larger spread for any given shower than the number of particles. This is illustrated in figures 1 and **??** which show the energy deposited and the number of charged particles in simulated EM showers using the GEANT4 program [**?**].

This shows both estimates show good linearity. Figure 3 shows the resolution in the two cases where it is clear the number of charged particles gives a very significant improvement, by almost a factor of two, in the intrinsic resolution.

These results motivate the development of a sensor which is capable of estimating the number of charged particles in a shower. The method considered here is to propose an ECAL with binary readout, such that each pixel of the calorimeter gives a yes/no result to the presence of a charged

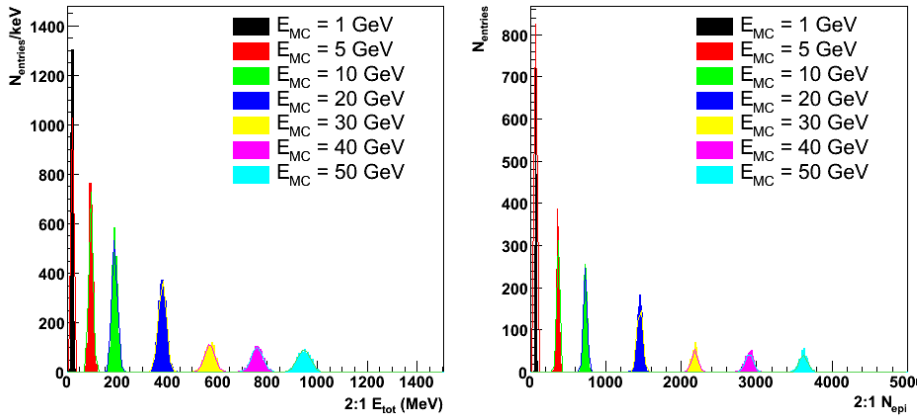

Figure 1: Comparison of the distributions of the quantity measuring shower energy using (left) energy deposited in the sensitive layers and (right) the number of charged particles crossing the sensitive layers.

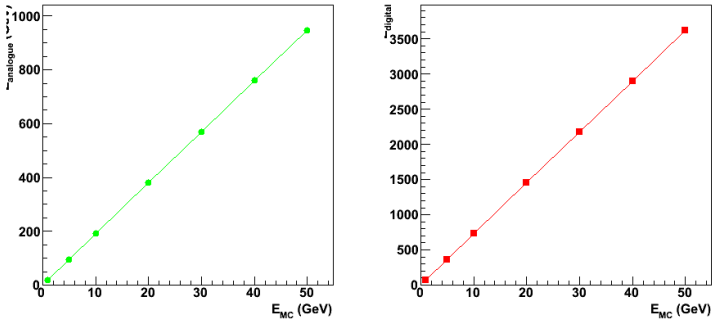

Figure 2: Comparison of the linearity as a function of shower energy, when meauring shower energy using energy deposited in the sensitive layers and the number of charged particles crossing the sensitive layers.

particle. Any charged particle gives an average energy deposit which has a universal minimum at a particular particle velocity and for normal incidence. Any other speed or incident angle gives a larger mean deposit, so a threshold set below the minimum ionising particle (MIP) level, allowing also for the Landau spread, should be efficient for detecting all charged particles.

To give an accurate estimate, such a sensor will need to have a low probability of two charged particles crossing the same pixel. The density of charged particles at the layer where it reaches a maximum for 100 GeV EM showers is shown in figure 4.

The peak value of XXX mm^{-2} therefore requires a pixel size smaller than YYY mm^2. The sensor discussed in the rest of this paper has a pixel size of $2.5 \times 10^{-3}\,\mathrm{mm}^2$, implemented as a square pixel of size $50 \times 50\,\mu\mathrm{m}^2$.

2.2 ILC requirements

As shown above, the pixel size for a binary ECAL need to be of the order of $50\,\mu$m. This is two orders of magnitude smaller than any of the analogue pad ECAL being considered for the ILC [**?**] and will be more than sufficient to allow PFA separation of particles. The size of the ECALs assumed in the ILC detector studies [**?**][**?**] is large with a total sensor surface area of

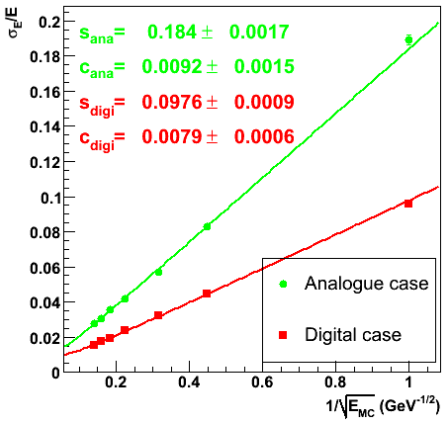

Figure 3: Comparison of the resolution as a function of shower energy, when meauring shower energy using energy deposited in the sensitive layers and the number of charged particles crossing the sensitive layers.

Figure 4: Distribution of peak density of charged particles within 100 GeV EM showers.

$\sim 2000\,\mathrm{m}^2$. For $50\,\mu$m pixels, this would require a total of $\sim 10^{12}$ pixels. This has been labelled the "tera-pixel" ECAL.

The ILC will run with "bunch trains", whereby the beams will collide ("bunch crossing") at a rate of around 200 ns but only for a short time, of around 1 ms, a bunch train. Each bunch train therefore contains around 5000 bunch crossings. The bunch train rate will be around 5 Hz, meaning that there are around 199 ms with no beam collisions following each bunch train. Hence, the ILC detectors will buffer data during the 1 ms bunch train and then read out in the 199 ms of dead time.

The physics interaction rate for producing events of interest will be low; less than one per bunch train. There will be significant levels of background from the ILC machine itself, as well as low energy physics events. However, with such a large number of pixels in a binary ECAL, then the overall data rate will be dominated by the rate of noise. Assuming a threshold of around five times the noise, then the noise rate would be $\sim 10^{-5}$ per pixel per bunch crossing. This means for the 5000 bunch crossings in a bunch train, each pixel has an average of ~ 0.05 hits. Hence, the sensor needs to be able to buffer at least this number of hits per pixel during the bunch train.

The one area where other sources of hits are not negligible will be in the most forward regions, where backgrounds from the machine can be substantial. A simulation using GUINEAPIG [**?**] shows a rate of hits of XXX, as shown in figure 5.

Figure 5: Machine background distribution in the endcap regions.

2.3 Other issues

An ECAL designed to deliver good PFA performance will also need to be compact, minimising any gaps between the converter layers. This keeps the transverse spread of the EM showers small, measured by the effective Molière radius, as this helps separate particles close to each other in jets. Hence, the sensitive layers have to be thin compared to the converter thicknesses. For example, tungsten has a radiation length of $x_0 = 3.5\,\mathrm{mm}$. most ILC ECAL designs have only $\sim 0.3X_0$ in each of the first few layers, which therefore corresponds to $\sim 1\,\mathrm{mm}$ of tungsten.

The compactness requirement also significantly limits the amount of cooling infrastructure which can be included between the converter layers. Any pipework will increase the space, degrading the effective Molière radius. Hence, this requires very low power sensors and readout electronics. The timing structure of the ILC means there are significant gains to be made by powering off any parts of the sensors which are not required during the 199 ms dead period. Even including this reduction of ~ 200 in power consumption, the requirements are tight. For example, one design [**?**] has no active cooling in the bulk of the ECAL, relying purely on conduction through the converter material and the electronics PCBs. The target power consumption for this design is $1\,\mathrm{mW/cm^2}$ (CHECK!).

A very significant issue with all such calorimeters is cost. With a sensitive area of $2000\,\mathrm{m^2}$, then the total cost will be dominated by the silicon detectors themselves. Hence, there is a strong motivation to reduce the sensor unit area cost. This pushes for simple sensors which can be produced through a large number of vendors and require no unusual processing features.

2.4 The TPAC sensor

In this paper, we present results from a test sensor which was designed to investigate a binary ECAL approach. The sensor is based on a $0.18\,\mu$m CMOS process, which was modified to include a "deep p-well" implant. This modified process is called INMAPS and is described elsewhere [**?**]. This protects signal charge from absorption by the circuit electronics and so allows a significant amount of signal processing and data handling in the pixels.

3 Design - ~ 10 pages

3.1 Overall architecture

Top-level overview.

Figure 6: Sensor overall architecture.

3.2 Fabrication and INMAPS

$0.18\,\mu$m CMOS INMAPS process.

3.3 Pre-shaper pixel

Circuit, parameters.

Mode of operation.

Figure 7: Pre-shaper pixel circuit.

3.4 Pre-sampler pixel

Circuit, parameters.

Figure 8: Pre-sampler pixel circuit.

Mode of operation.

3.5 Mask and trim configuration

Operation. Load method. Readback.

3.6 Data storage

Memory operation. Dead area. Memory limit.

3.7 Readout

Operation of readout columns. Speed limitation.

3.8 Known design issues

Details of three bugs. Crosstalk and power.

3.9 DAQ system and operation

USB_DAQ and support PCB. Bonding and yield issues. Operating parameters for all following measurements are 400 ns bunch crossings. Grounding of substrate.

4 Single pixel performance - ~ 10 pages

4.1 Circuit simulation

Expected noise, gain.

Figure 9: Simulation of noise.

4.2 Charge spread simulation

The signal from a minimum ionising particle (MIP) arises as the particle passes through the epitaxial layer of the sensor. A relativistic charged particle will create an average of 80,electron-hole pairs per micron in silicon, although there are fluctuations around this value, as described by the Landau function **??**.

Physically, the electron-hole pairs are created throughout the silicon sensor, but only within (or near) the epitaxial layer are the liberated electrons able to diffuse to the collecting diodes and hence be seen as signal. Hence, in a 15 μm thick epitaxial layer, then for a particle at normal incidence to the sensor, it might be expected that around 1200 e^- will be available to contribute to the signal.

However, some electrons from the substrate close to the epitaxial layer can also diffuse into the epitaxial layer and so be collected. Conversely, electrons in the deep p-well implant will tend to be lost. More importantly, the charge will diffuse and so may be absorbed by the collection diodes of the neighbouring pixel. Finally, other n-well structures can collect the charge and hence it will be lost in terms of being signal. This last effect is the reason for which the deep p-well implant was developed.

To estimate these effects quantitatively, a simulation of the sensor pixel was performed using the Sentaurus **??** package. The pixel design file was used as input, ensuring the details of the pixel were correctly simulated. Charge equivalent to that expected for a MIP was deposited at various locations within the pixel and then simulated to investigate where it was absorbed or lost. A 3×3 array of pixels were simulated, from the sensor surface down to 32 μm below ($150 \times 150 \times 32\,\mu\text{m}^3$ in total) to allow for neighbour pixel charge collection. The simulation was time-consuming so a limited subset of positions were simulated. Because of the approximate eight-fold rotational symmetry of the sensor, all positions simulated were within a triangle with the pixel centre, corner, and side centre as its three corners. Within this triangle, the positions simulated were spaced 5 mum apart, resulting in 21 points in total. Using the symmetry, these could be translated and rotated to give a 5 μm regular array across the whole of the central pixel.

The simulation results are shown in figure 10 for sensors with and without deep p-well.

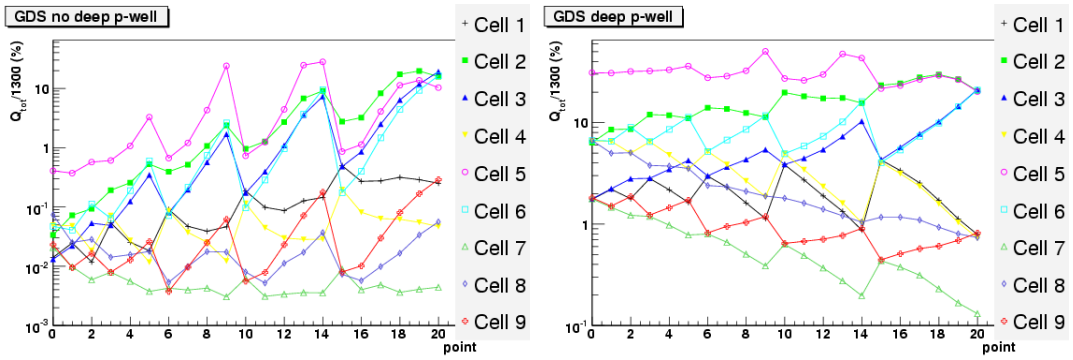

Figure 10: Simulation of charge spread for (left) no deep p-well and (right) deep p-well

Overall efficiency for MIP vs. threshold.

4.3 Test pixel performance

The sensor included three test pixels outside of the 168×168 "bulk" array. Several internal nodes of two of these pixels were accessible externally, allowing analogue measurements of their levels.

EQUIPMENT USED, AMP ETC.

Analogue noise,

A laser operating at a wavelength of 1064 nm was used to inject a controllable signal level into the text pixels. Due to the high fraction of coverage in each of the six metal layers, it was not possible to illuminate the sensor from the top surface so the laser was directed at the

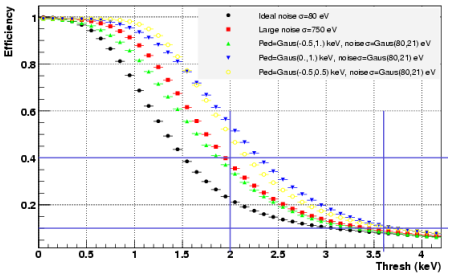

Figure 11: Simulation of efficiency vs. threshold.

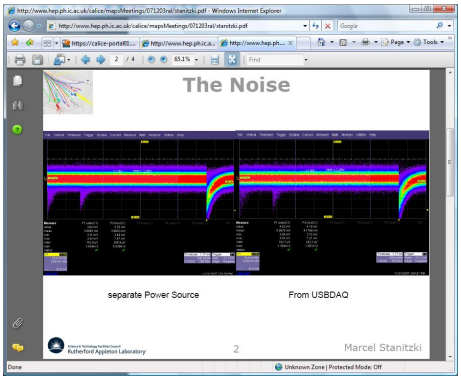

Figure 12: Test pixel noise.

substrate. The laser focus was adjusted to compensate for the substrate thickness and refractive index, giving a spot size in the epitaxial layer of approximately XXX μ.

gain (from laser),

Figure 13: Test pixel laser signal.

To get an absolute calibration of the signal size, the sensor was exposed to an intense ^{55}Fe source. This isotope produces γ radiation with a photon energy of 5.9 keV. Photons of this energy can deposit all the energy within a small O(1 μm^3) volume within the silicon. As shown above, in most cases, it would be expected that a significant fraction of the charge would diffuse out of the test pixels or be absorbed. However, a small number of the γ particles will interact directly under the collection diodes **??**. In this case, effectively all the charge liberated, around 1600 e^-, will be collected by the diode, giving a well-defined signal size.

calibration of pre-samplers gain (from ^{55}Fe);

To study the signal charge diffusion in the epitaxial layer, the laser was scanned over the surface of the test pixels in 5 μm steps and the averaged analogue signal for 1000 (CHECK) pulses was recorded using the oscilloscope. This gives a map of the charge seen in the two test pixel which can be read out as a function of the injected charge position. This can be directly compared with the simulated charge diffusion described above, although a correction for the laser spot size of XXX μm is applied to the simulation. The measurements were performed for sensors both with and without deep p-well.

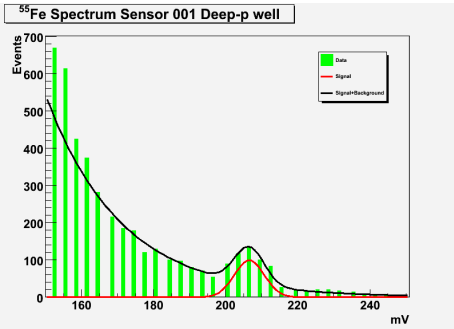

Figure 14: Test pixel ^{55}Fe signal.

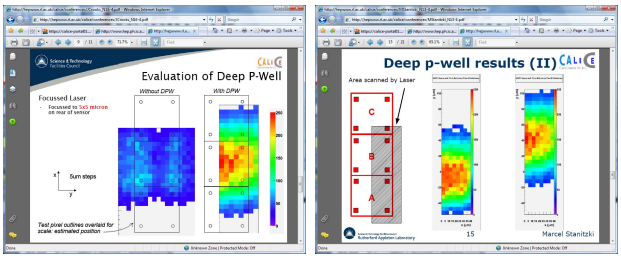

Figure 15: Test pixel charge spread.

4.4 Bulk pedestal and noise

The performance in the bulk pixels is less straightforward to measure as there is no analogue readout available. However, the rate of hits in each pixel as a function of the applied threshold effectively allows the integral of the analogue spectrum to be measured and hence the spectrum itself can be estimated. The results in this section are based on performing such "threshold scans" and measuring the response.

One complication is that pickup was observed between pixels when O(100) were enabled and firing at the same time, see Section 5. This is not a major problem when operating the sensor for its design purpose as only a few pixels are expected to fire in each event. However, for the basic performance measurements presented below, the pickup would prevent the response of individual pixels from being measured. Hence to remove this sensor-wide effect, only small number of pixels are unmasked at any time for the following results.

A threshold scan performed with no external stimulus will result in a hit rate peaked near the pixel pedestal. The result for a typical pixel is shown in figure 16. The resulting distribution is well described by a Gaussian and so can be characterised by the mean and root mean square (RMS). The mean gives the pedestal for the pixel and the RMS gives the noise, in units of the threshold setting, "threshold units" (TU).

The distribution of the pixel mean and RMS values for the two preShaper quadrants of a typical sensor are shown in figure 17. It is seen that there is a significant spread of pedestals with a quadrant. The pedestal RMS is around 40 TU. This is much bigger than the noise on the pixels, which has an average value of around 5 TU for quadrant 0 and 6 TU for quadrant 1.

The value of the pedestal and noise for each pixel as a function of the position within the sensor is shown in figure 18. The values of the pedestals and noise show no correlation with position within the sensor and appear genuinely random.

The spread of pedestals can be reduced using the per-pixel trim setting. This allows a value in the range 0-15 to be loaded to each pixel to adjust the pedestal position. The effect of this

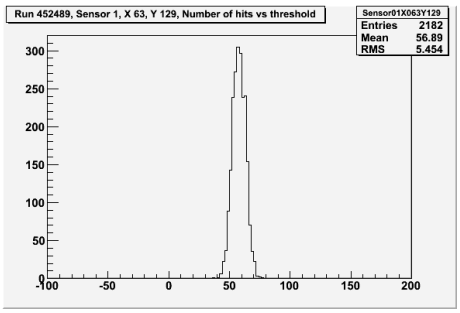

Figure 16: Typical channel threshold scan.

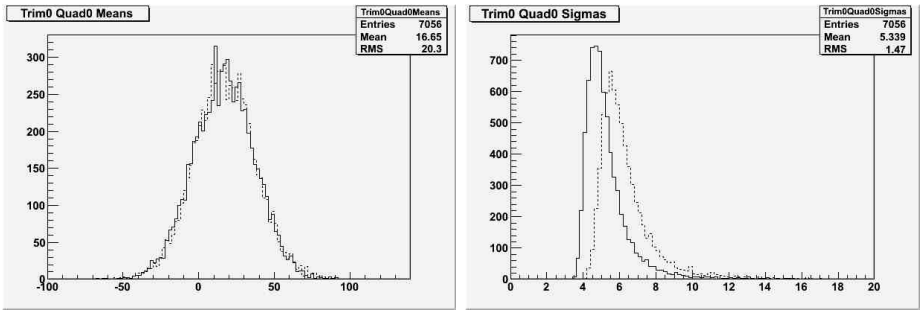

Figure 17: Distributions of (left) pedestals and (right) noise for quadrant 0 (solid histogram) and 1 (dashed histogram), in threshold units, for a typical sensor.

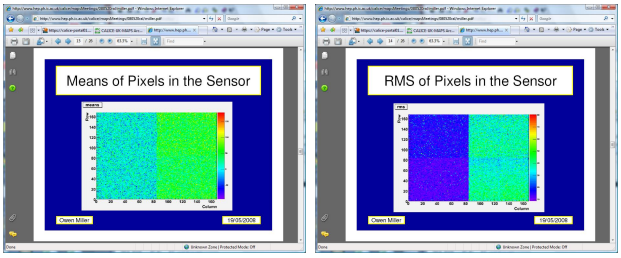

Figure 18: Two-D map of (left) pedestals and (right) noise for a typical sensor.

on pedestal of a typical pixel is shown in figure 20.

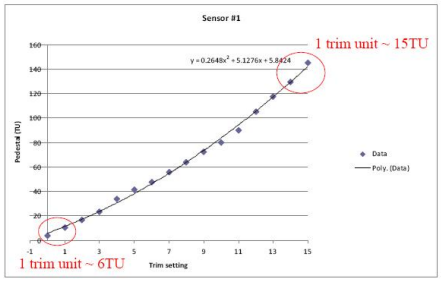

Figure 19: Typical channel trim scan.

The spread of pedestals before and after trimming a typical sensor is shown in figure **??**. It is seen that the RMS of the pedestals is reduced by a factor of five. The resulting spread is around the size of the per pixel noise and so gives a non-negligible contribution to the apparent noise when setting a common pedestal for all pixels. This effect is limited by the number of trim bits available. With four bits, then a granularity of the trim of 16 values is possible. However, the spread of the pedestals is around 100 TU, so that even with careful matching of the trim range, the trim LSB would be around 6 TU. Two additional trim bits will be implemented in a future version of the sensor.

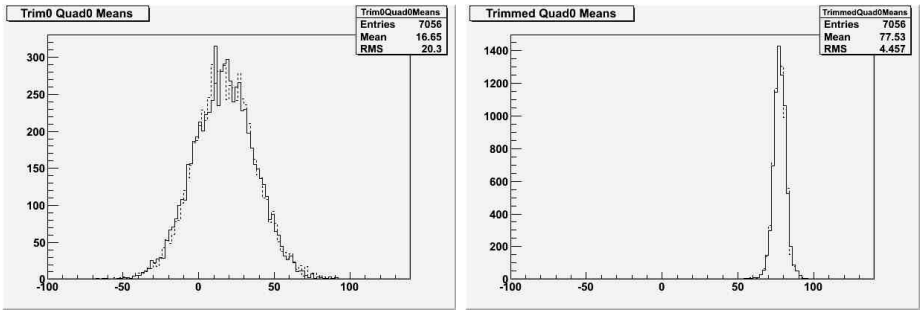

Figure 20: Pedestals in quadrants 0 (solid line) and 1 (dashed line) for (left) a trim setting of 0 for all pixels and (right) a optimised per-pixel trim setting, for a typical sensor. The left plot is the one shown in figure 17

The pixel noise can be influenced by several factors. The sensors are operated with no explicit bias connection to the substrate. This could in principle allow environmental noise pickup. The distribution of noise for the two preShaper quadrants both with and without the substrate being grounded as shown in figure 21. It is seen that leaving the substrate unconnected has no significant effect on the noise.

Figure 21: Noise for with (solid histogram) and without (dashed histogram) grounding the substrate for (left) quadrant 0 and (right) quadrant 1.

Effect of resets at start of bunch train.

4.5 Bulk laser signal response

A similar system to that described above was used to illuminate the sensor using a laser of wavelength 1064 nm. In this case, the signal was injected into the bulk pixel area and the respose measured using a threshold scan. A typical response is shown in figure 22, where the laser signal is clearly seen. The actual size of the laser signal was found by fitting the falling edge of the response curve to an integrated Gaussian (erf) function. This gives a pseudo-analogue signal response estimate from the mean of the Gaussian and an estimate of the noise from the sigma.

Effect of focus and hence substrate tilt.

Optimisation of S/N with biases.

Gain (from laser),

calibration of bulk pre-samplers and pre-shapers; compared to simulation.

Laser charge spread vs. position; compared to simulation with and without deep p-well.

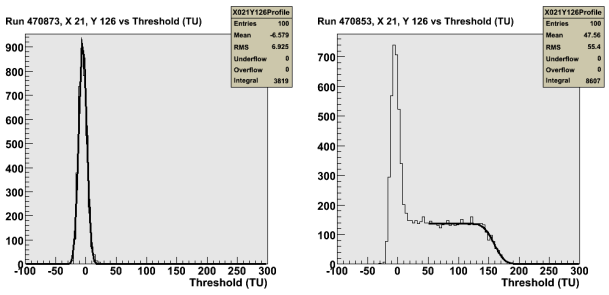

Figure 22: Threshold scan (left) without and (right) with laser.

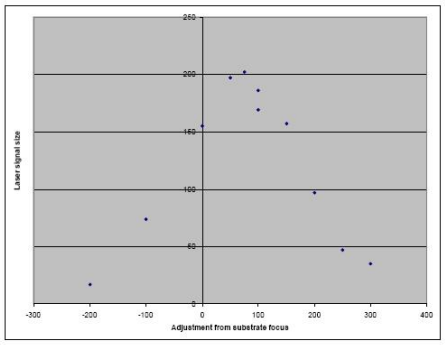

Figure 23: Signal size vs laser focus.

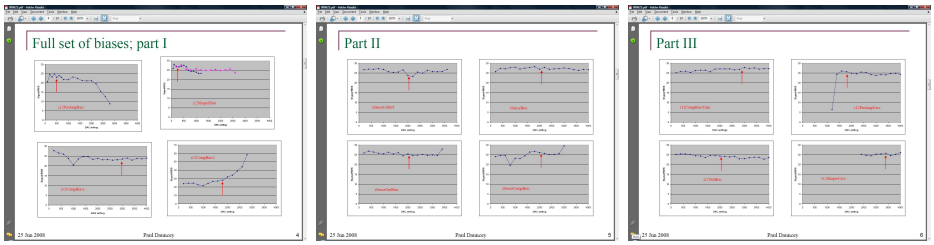

Figure 24: Laser signal/noise as a function of various bias DAC settings.

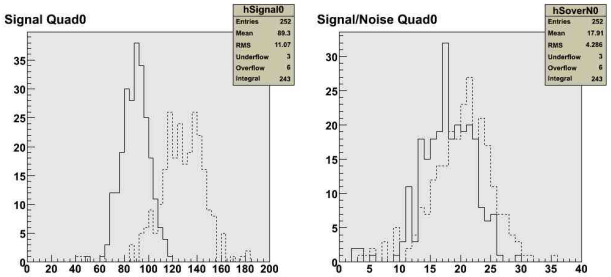

Figure 25: Laser (left) signal and (right) signal/noise for quadrants 0 (solid line) and 1 (dashed line).

5 Sensor performance - ~ 10 pages

5.1 Configuration load

Error rates from sensor load.

Figure 26: Two-D map of laser gain for typical sensor.

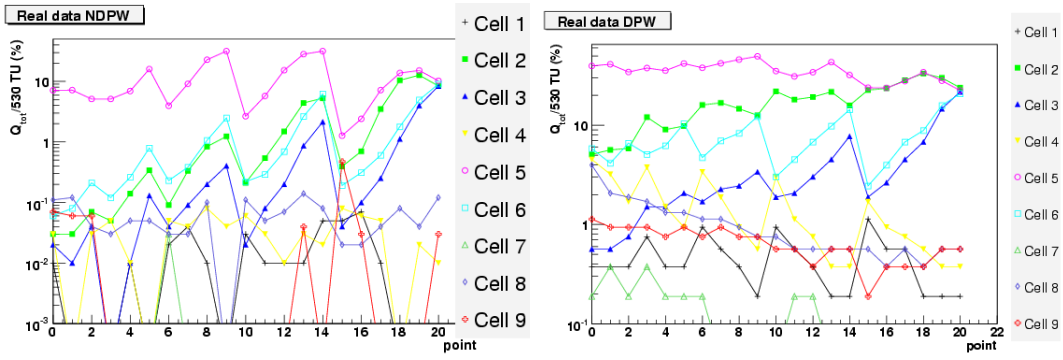

Figure 27: Charge seen at each impact point for each pixel (right) without deep p-well and (left) with deep p-well.

5.2 Noise and crosstalk

Crosstalk;

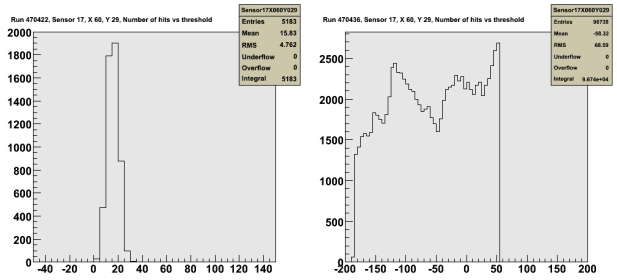

Figure 28: Effect of crosstalk on typical pixel (left) single pixel enabled (right) all pixels enabled.

dependence on masking, position.

Figure 29: Onset of crosstalk as number of unmasked channels increases.

Single pixel plots in 4 done with only pixel studied unmasked.
Possible cause of crosstalk, how to fix.

5.3 Hit corruption

Twinning, corruption rates using hitOverride.

5.4 Source response

Efficiency vs threshold for ^{90}Sr.
Calibration peak for ^{55}Fe).

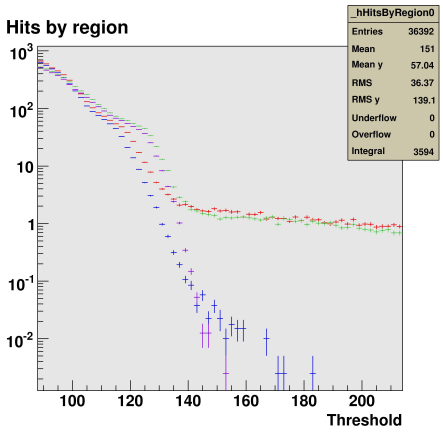

Figure 30: Rate of hits vs threshold for ^{90}Sr.

Figure 31: Rate of hits vs threshold for ^{55}Fe.

5.5 Beam test

DESY, Dec 2007 for one week. Around 100 runs, XXX TBytes. Explain ran with no trim, crosstalk, high threshold.

As a tracker; residuals.

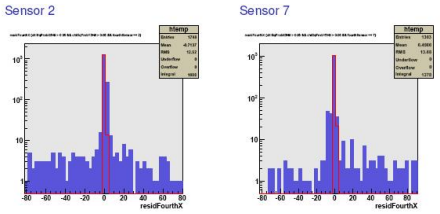

Figure 32: Residuals on inner sensors.

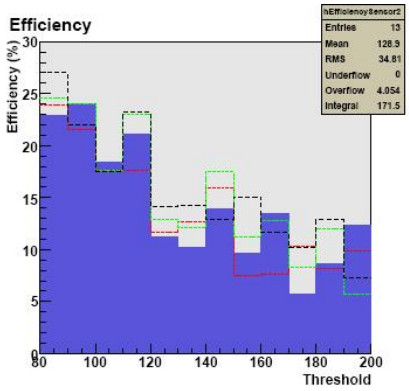

Figure 33: Efficiency vs threshold.

Measure pedestal separately, correct to "real" threshold. Relative efficiency vs real threshold, comparing real threshold distribution for all and for hit pixels.

Figure 34: Distribution of real thresholds for all and hit pixels.

Figure 35: Relative efficiency vs real threshold.

5.6 Cosmics

Absolute MIPS efficiency

Figure 36: Efficiency vs real threshold.

6 Physics performance - ~ 5 pages

6.1 Simulation

GEANT4 and Mokka. Verified using general CALICE beam test.

6.2 MIP counting

Weighting of neighbours.

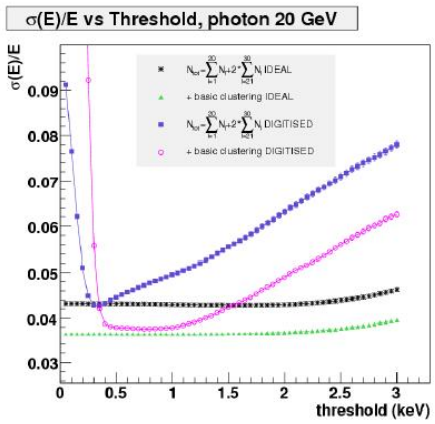

Figure 37: Effect of MIP counting.

6.3 Electromagnetic shower resolution

Resolution with and without INMAPS deep p-well.

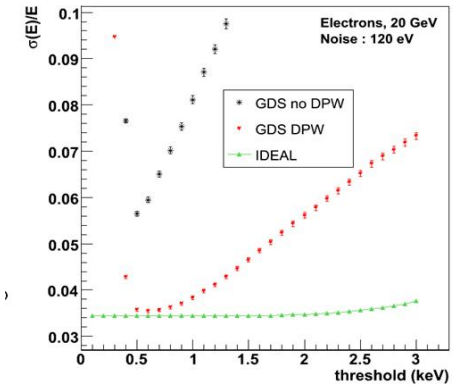

Figure 38: Resolution with and without deep p-well including MIP counting.

6.4 Hadronic jet resolution

No-harm case.

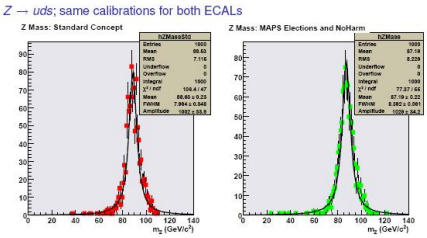

Figure 39: Hadronic jet resolution for "no-harm" case.

Improvements.

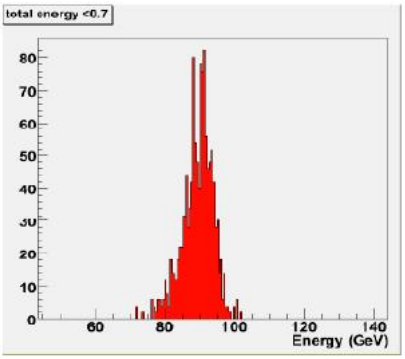

Figure 40: Hadronic jet resolution with PFA-improved algorithm.

7 Conclusions - ~ 2 pages

Proven INMAPS deep p-well. Proven pixel design adequate. Proven DECAL will work better than AECAL.

Need work on overall sensor crosstalk and trims/pedestal variations.